



# Theoretical model for annular flow condensation in rectangular micro-channels

Sung-Min Kim, Issam Mudawar\*

Boiling and Two-Phase Flow Laboratory (BTPFL) and Purdue University International Electronic Cooling Alliance (PIIECA), Mechanical Engineering Building, 585 Purdue Mall, West Lafayette, IN 47907-2088, USA

## ARTICLE INFO

### Article history:

Received 30 April 2011

Received in revised form 24 June 2011

Accepted 24 June 2011

Available online 25 October 2011

### Keywords:

Condensation  
Micro-channel  
Annular model  
Eddy diffusivity

## ABSTRACT

This study examines the pressure drop and heat transfer characteristics of annular condensation in rectangular micro-channels with three-sided cooling walls. A theoretical control-volume-based model is proposed based on the assumptions of smooth interface between the annular liquid film and vapor core, and uniform film thickness around the channel's circumference. Mass and momentum conservation are applied to control volumes encompassing the liquid film and the vapor core separately. The model accounts for interfacial suppression of turbulent eddies due to surface tension with the aid of a new eddy diffusivity model specifically tailored to shear-driven turbulent films. The model predictions are compared with experimental pressure drop and heat transfer data for annular condensation of FC-72 along  $1 \times 1 \text{ mm}^2$  parallel channels. The condensation is achieved by rejecting heat to a counterflow of water. The data span FC-72 mass velocities of 248–367  $\text{kg/m}^2 \text{ s}$ , saturation temperatures of 57.8–62.3  $^\circ\text{C}$ , qualities of 0.23–1.0, and water mass flow rates of 3–6 g/s. The data are also compared to predictions of previous separated flow mini/micro-channel and macro-channel correlations. While some of the previous correlations do provide good predictions of the average heat transfer coefficient, they fail to capture axial variation of the local heat transfer coefficient along the channel. The new model accurately captures the pressure drop and heat transfer coefficient data in both magnitude and trend, evidenced by mean absolute error values of 3.6% and 9.3%, respectively.

© 2011 Elsevier Ltd. All rights reserved.

## 1. Introduction

Most of the phase-change electronic cooling research published during the past three decades has been focused on removing heat from the electronic device using micro-channel heat sinks, jet-impingement or sprays [1–5]. Far less emphasis has been placed on high-flux heat rejection from the two-phase cooling system. A key reason behind this trend is a common perception that a commercial condenser can always be found to reject the heat from virtually any phase-change cooling system. However, recent studies concerning very high power density defense electronics have shown that substantial enhancement in heat dissipation from the device can be achieved by using a two-loop cooling system [6,7]. Here, a primary cooling loop is used to extract the heat from the device by highly subcooled flow boiling, and the heat is rejected via a high performance heat exchanger to a separate low-temperature refrigeration loop. Compact and lightweight system design requires that the intermediate condenser achieve heat fluxes comparable to those of the flow boiling module.

Because condensation heat transfer coefficients are typically much smaller than those realized with subcooled flow boiling,

commercial condensers are often far too large to meet the size and packaging constraints of defense electronics. The present study concerns the design of a relatively new class of condensers that employ a series of micro-channels to meet the stringent size and weight requirements of defense electronics. Another goal is to maintain mostly annular flow along the micro-channels to capitalize upon the large condensation heat transfer coefficients associated with thin films. With superheated or saturated inlet conditions, a very thin film is initiated in the upstream region of the channel, which is driven along the channel by the shear stresses exerted by the core vapor flow. Micro-channels greatly increase vapor velocity and therefore the shear stress exerted upon the film interface. This greatly decreases the film thickness, resulting in very high condensation heat transfer coefficients. However, the film thickness increases along the micro-channel as an increasing fraction of the vapor flow condenses into liquid. Eventually, the annular regime collapses and is replaced by a succession of thermally less efficient slug, bubbly, and liquid flow regimes. While micro-channels do enhance heat transfer performance, they also increase pressure drop. Therefore, the design of micro-channel condensers requires predictive tools for both pressure drop and condensation heat transfer coefficient.

The vast majority of published studies addressing the prediction of pressure drop and condensation heat transfer coefficient for annular flows are based on semi-empirical separated flow correlations

\* Corresponding author. Tel.: +1 (765) 494 5705; fax: +1 (765) 494 0539.

E-mail address: [mudawar@ecn.purdue.edu](mailto:mudawar@ecn.purdue.edu) (I. Mudawar).

URL: <https://engineering.purdue.edu/BTPFL> (I. Mudawar).

**Nomenclature**

$A$	area	$u^*$	friction velocity
$A^+$	constant in Eq. (30)	$W_{ch}$	micro-channel width
$A_{f,*}$	flow area of liquid control volume	$W_s$	width of solid wall separating micro-channels
$c_p$	specific heat at constant pressure	$x$	quality
$D_h$	hydraulic diameter	$y$	distance perpendicular to channel wall
$F$	function	$y^+$	dimensionless distance, $yu^*/\nu_f$
$f$	Fanning friction factor	$z$	stream-wise distance
$G$	mass velocity		
$g$	gravitational acceleration		
$h$	enthalpy; heat transfer coefficient	<i>Greek symbols</i>	
$H_{ch}$	micro-channel height	$\beta$	channel aspect ratio, $W_{ch}/H_{ch}$
$h_{fg}$	latent heat of vaporization	$\Gamma_{fg}$	rate of mass transfer due to condensation
$K$	Von-Karman constant	$\delta$	thickness of condensing film
$l^*$	turbulent mixing length	$\delta^+$	dimensionless thickness, $\delta u^*/\nu_f$
$MAE$	mean absolute error	$\varepsilon_h$	eddy heat diffusivity
$\dot{m}$	mass flow rate	$\varepsilon_m$	eddy momentum diffusivity
$N$	number of micro-channels in test section	$\mu$	dynamic viscosity
$n$	turbulence dampening exponent	$\nu$	kinematic viscosity
$P$	pressure	$\rho$	density
$\Delta P$	pressure drop	$\sigma$	surface tension
$P_f$	perimeter	$\tau$	shear stress
$Pr$	Prandtl number	$\tau_i^*$	dimensionless interfacial shear stress
$Pr_T$	turbulent Prandtl number		
$q''$	heat flux at distance $y$ from micro-channel wall	<i>Subscripts</i>	
$q''_{base}$	heat flux based on total base area of micro-channel condenser	$c$	vapor core
$q''_w$	heat flux based on micro-channel's cooled perimeter	$exp$	experimental (measured)
$Re$	Reynolds number	$f$	saturated liquid; liquid film
$T$	temperature	$g$	saturated vapor; vapor core
$T^+$	dimensionless temperature	$i$	interfacial
$u$	velocity	$pred$	predicted
$u^+$	dimensionless velocity	$sat$	saturation
		$tp$	two-phase
		$tr$	transition for laminar to turbulent flow

(mostly Lockhart–Martinelli-type [8]) and empirical heat transfer correlations (e.g., [9]), respectively. Like all correlations, these predictive tools are valid only for the range of operating conditions of databases these correlations are based upon. This limitation has created a need for development of theoretical models that possess a broader application range. Theoretical control-volume-based models have been quite effective in predicting both pressure drop [10] and heat transfer [11] in saturated flow boiling in micro-channel heat sinks, subcooled flow boiling pressure drop in micro-channel heat sinks [12], and flow boiling critical heat flux [13]. Nonetheless, several fundamental challenges remain when attempting to develop an accurate model for annular two-phase flow. These include interfacial instabilities, interfacial mass, momentum and heat transfer, and turbulence within the annular film.

One source of difficulty in modeling annular two-phase flow is interfacial waves [14–20]. These are highly complex phenomena and no effective method has been developed for their characterization. One type of waves is ripples, which are characterized by both small amplitude and small wavelength and do not contribute substantially to liquid film mass transport. Large waves can also develop, where the perturbed liquid film is replaced by lumps of liquid that are separated by a thin layer of liquid. Due to their appreciable protrusion into the vapor flow, the motion of large waves can be dominated more by vapor drag forces than by interfacial vapor shear. Modeling large waves is complicated by the fact that they are highly nonlinear forms of instability that greatly complicate the effectiveness of averaging methods to predict the liquid film's momentum or heat transfer transport behavior. Despite extensive efforts to assess the influence of interfacial waves on mass,

momentum and heat transfer, no systematic tools have been developed to effectively model this influence.

Two other phenomena that complicate the development of accurate annular flow models are droplet entrainment and droplet deposition. These two phenomena are closely related to interfacial waviness. Entrainment refers to tiny liquid droplets that break off the crests of waves and are driven along with the vapor core. Deposition refers to droplets from the vapor core falling back upon the film interface. In their study of annular film evaporation, Qu and Mudawar [10] proved that droplet entrainment and deposition play a very important role in micro-channels compared to macro-channels.

Another challenge in modeling annular flows is accurate prediction of turbulent or eddy diffusivity within the annular liquid film. Classical turbulence models are known to break apart when dealing with fluid regions near a vapor–liquid interface [19–21]. As discussed by Mudawar and El-Masri, surface tension forces along the interface can significantly dampen turbulent eddies, resulting in appreciable resistance to heat transfer near the interface. Ignoring this effect could result in appreciable error in predicting the condensation heat transfer coefficient.

The present study is a follow-up to a recent study by the authors that explored condensation of FC-72 along parallel, square micro-channels [22,23]. Using high-speed video imaging and photomicrographic techniques, five distinct flow regimes were identified: smooth-annular, wavy-annular, transition, slug, and bubbly, with the smooth-annular and wavy-annular regimes being most prevalent. Both homogeneous and Lockhart–Martinelli-type separated flow models were assessed for pressure drop prediction. Similarly,

prior correlations for condensation heat transfer in both macro and micro-channels were assessed against the new FC-72 data, and a new correlation was developed that showed excellent predictive capability based on both the new FC-72 data and a large database for mini/micro-channel flows amassed from eight previous sources.

The primary goal of the present study is to develop a theoretical control-volume-based model for annular condensing micro-channel flows. Addressed in the development of this new model are the effects of droplet entrainment and deposition, interfacial instabilities, and dampening of liquid film turbulence near the liquid–vapor interface. The model’s predictive accuracy is assessed against the FC-72 pressure drop and heat transfer data measured previously by the authors [22,23], and compared to those of prior annular condensation correlations.

**2. Experimental methods**

**2.1. Test facility**

Fig. 1(a) shows a schematic of the two-phase experimental facility constructed for this study. It consists of a primary FC-72 loop and secondary water loop. FC-72 from a reservoir is circulated in the primary loop with the aid of gear pump. The FC-72 liquid passes through a set of flow meters followed by an in-line electric heater before entering the condensation module. The inline electric heater is used to bring the FC-72 to slightly superheated state at the inlet to the condensation module. A plate-type heat exchanger is used to bring any vapor exiting the test module to liquid state.

The FC-72 is condensed along the condensation module by rejecting heat to a counter-flow of water being circulated in the secondary loop. The hot water is brought back to near room temperature by rejecting the absorbed heat via a Lytron modular cooling system. Exiting the Lytron system, part of the water flow is

returned to the condensation module while the balance is supplied to the plate-type heat exchanger. The secondary loop also includes a set of flow meters for flow rate measurement.

**2.2. Condensation module**

Fig. 1(b) and (c) show the construction of the micro-channel condensation module. The module consists of a cover plate, housing, condensation copper block, and water channels. The cover plate, which seals the tops of the micro-channels, is made from transparent polycarbonate (Lexan) to facilitate photographic study of the condensing flow. The top of the copper block has a 2-cm wide by 30-cm long heat transfer area. Ten 1-mm square micro-channels are machined into the top surface. The water flows through three parallel 3.8-mm brass channels that are soldered to the underside of the copper block. The copper block is inserted into a rectangular G-10 housing that features FC-72 inlet and outlet ports, micro-channel inlet and outlet plenums, and pressure and temperature measurement ports.

**2.3. Experimental results**

The experimental study consisted of 24 separate experiments, corresponding to a test matrix of six FC-72 different mass velocities ( $G = 68, 118, 186, 248, 306, \text{ and } 367 \text{ kg/m}^2\text{s}$ ) and four different water flow rates ( $\dot{m} = 3, 4, 5, \text{ and } 6 \text{ g/s}$ ). Operating conditions were set to achieve mostly annular flow near the inlet of the micro-channels. The FC-72 was introduced into the condensation module in pure vapor state with a quality of 1.11–1.17 for low FC-72 mass velocities ( $G = 68\text{--}186 \text{ kg/m}^2\text{s}$ ), and 1.08–1.10 for high FC-72 mass velocities ( $G = 248\text{--}367 \text{ kg/m}^2\text{s}$ ). These conditions resulted in an upstream single-phase superheated vapor region 1.1–3.1 cm-long (4–10% of the total channel length) for the low

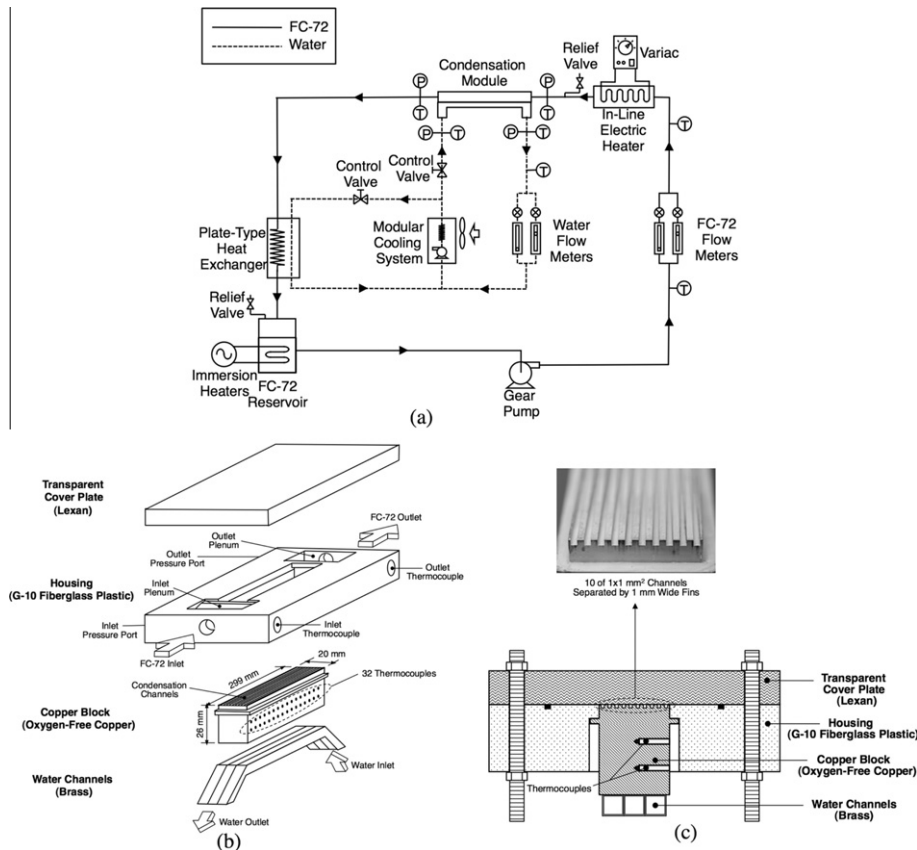


**Fig. 1.** (a) Schematic diagram of test loop. (b) Construction of micro-channel condensation module. (c) Cross-sectional view of condensation module.

FC-72 mass velocity range, and 2.7–5.8 cm (9–19% of the total channel length) for the high FC-72 mass velocity range. The inlet plenum pressure ranged from 1.040–1.324 bar. Operating conditions along the channel length were as follows: saturation temperature range of  $T_{sat} = 57.2\text{--}62.3\text{ }^{\circ}\text{C}$ , quality range of  $x = 0\text{--}1.17$ , and heat flux range of  $q''_w = 0.43\text{--}3.21\text{ W/cm}^2$ .

As detailed in [22], heat loss through the cover plate is estimated at less than 2% of the heat input through the base of the micro-channels. All pressure transducers used in this study featured an accuracy of 0.05%. The rotameters had a flow rate accuracy of  $\pm 2\%$  of measurement.

Using a combination of high-speed video imaging and photomicrographic techniques, five distinct flow regimes (smooth-annular, wavy-annular, transition, slug, bubbly) were identified as depicted in Fig. 2. Fig. 3(a) and (b) show the variation of the measured local condensation heat transfer coefficient with quality for different FC-72 mass velocities at water mass flow rates of 3 and 6 g/s, respectively. The smooth-annular flow regime is initiated upstream with the formation of a very thin liquid film. The small thickness is responsible for the high values of convective heat transfer coefficient in the smooth-annular regime. Fig. 2 shows how increasing the FC-72 mass velocity increases the upstream span of the smooth-annular regime. The increased mass velocity also increases the magnitude of shear stress exerted upon the liquid film, which decreases the film thickness causing an increase in the heat transfer coefficient as depicted in Fig. 3(a) and (b). Increasing the mass flow rate of water increases the local rate of condensation, causing a thickening of the FC-72 liquid film, and a corresponding decrease in the heat transfer coefficient.

Further details of the experimental techniques used and of the pressure drop, and heat transfer results are provided by Kim et al. [22], and Kim and Mudawar [23], respectively.

### 3. Model development

#### 3.1. Key findings from flow visualization experiments

Qu and Mudawar [10] showed that droplet entrainment and deposition play a crucial role in mass, momentum and heat trans-

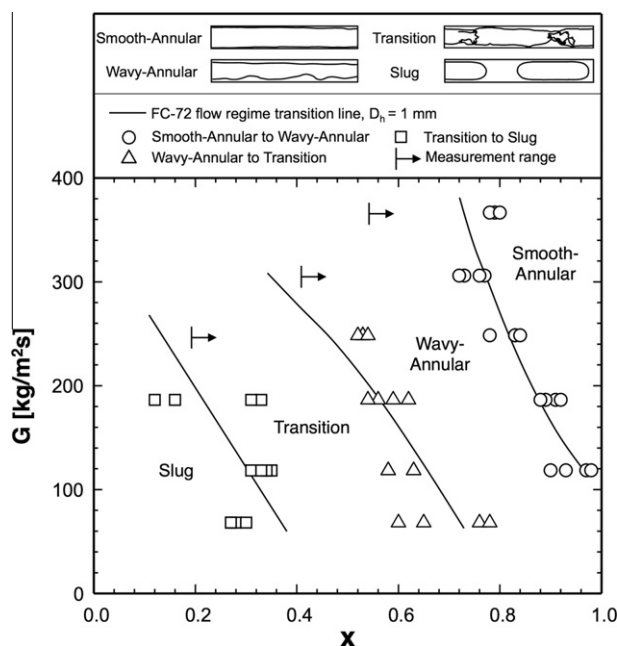


Fig. 2. Two-phase flow regime boundaries for condensation of FC-72 in square micro-channels with  $D_h = 1\text{ mm}$  (Kim et al., [22]).

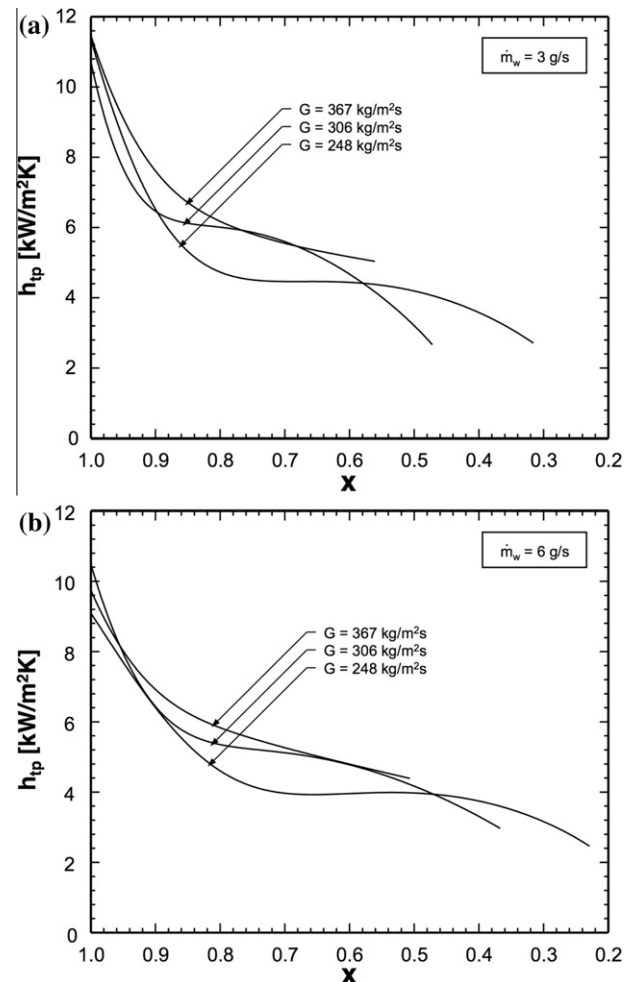


Fig. 3. Variation of measured local heat transfer coefficient corresponding to annular flow regime with FC-72 quality for different FC-72 mass velocities with (a)  $\dot{m}_w = 3\text{ g/s}$ , and (b)  $\dot{m}_w = 6\text{ g/s}$ .

fer in annular evaporating micro-channel flows. As shown in Fig. 4(a), droplets are formed by shattering of liquid from the micro-channel's upstream. However, the flow visualization results from the present authors' study have shown that no droplets are formed in the annular region of micro-channel condensing flow [22]. Therefore, these effects are neglected in the development of the present theoretical annular flow model.

The authors' recent micro-channel condensation studies also showed that the annular region consists of two distinct sub-regimes. The upstream, smooth-annular regime features a thin smooth liquid film. However, the annular film in the wavy-annular regime is marred by interfacial waves. Nonetheless, these waves were fairly sinusoidal in profile and do not shatter or produce entrained droplets, nor do they evolve into large waves as is commonly observed in annular macro-channel flows.

#### 3.2. Model assumptions

A key challenge in developing the theoretical model is determining the distribution of liquid along the channel's circumference. Gravity effects are negligible in micro-channels compared to macro-channels, given the large shear stresses encountered in the former. This precludes any preferential accumulation of liquid based on orientation of the flow relative to gravity. However, the surface tension of the working fluid can have a significant influence on the liquid distribution. Fig. 4(b) contrasts the liquid distribution

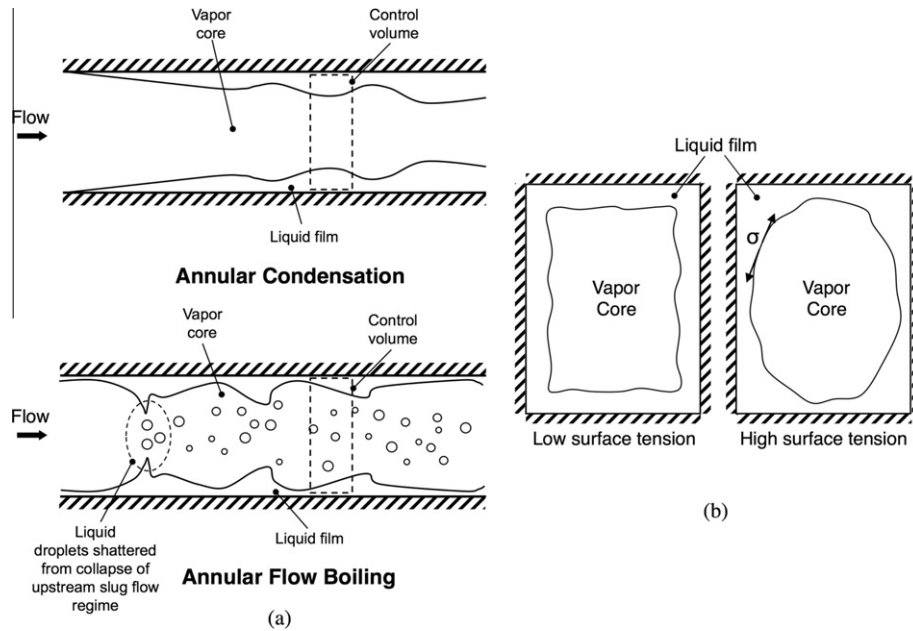


Fig. 4. (a) Fundamental differences between annular condensation and annular flow boiling in micro-channels. (b) Effects of surface tension on liquid distribution along channel perimeter.

in a rectangular micro-channel for the case of a very low surface tension fluid such as FC-72 (0.0084 N/m at 1 bar) compared to that of a relatively high surface tension fluid such as water (0.059 N/m at 1 bar). Notice how low surface tension fluids, which include most dielectric fluids used in electronic cooling applications, tend to maintain a nearly uniform liquid film thickness around the channel circumference. The present study will be based on this assumption since it concerns mostly low surface tension electronic cooling fluids.

Fig. 5 provides a schematic representation of liquid film condensation in a rectangular micro-channel with three-sided wall cooling and relevant nomenclature used in the development of the annular condensation model. Following are key assumptions of the model.

- (1) The annular condensing flow is steady, incompressible, and concurrent.
- (2) Gravitational effects are negligible.
- (3) Both entrainment and deposition of liquid droplets are negligible.

- (4) Pressure is uniform across the micro-channel's cross-sectional area.
- (5) Thermophysical properties are based on local saturation pressure.
- (6) Mean vapor velocity is assumed across the vapor core's cross-sectional area.
- (7) Mass transfer occurs only at the interface between the vapor core and the liquid film.
- (8) The liquid film interface is smooth.
- (9) Liquid film thickness is uniform around the channel's circumference.
- (10) Axial momentum changes in the liquid film are negligible.
- (11) The liquid film flow can be laminar or turbulent.
- (12) The circumferential heat flux is uniform along the vapor-liquid interface.

The boundary condition of base heat flux,  $q''_{base}$ , beneath the micro-channels is determined from local temperature measurements obtained by arrays of thermocouples embedded in two separate planes in the copper block [23]. The local temperatures in the cop-

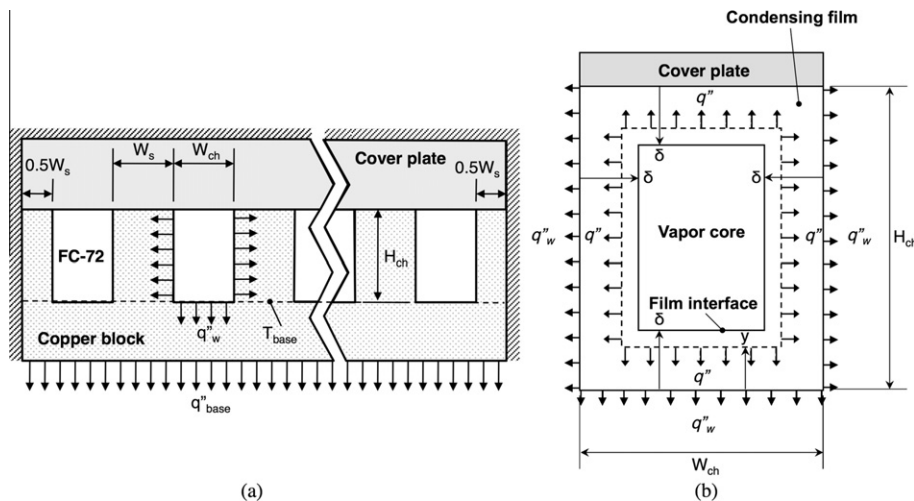


Fig. 5. Schematic representations of (a) condenser with rectangular micro-channels and (b) liquid film condensation in micro-channel with three-sided wall cooling.

per block are fitted to a third- or fourth-order polynomial function of stream-wise distance, and the corresponding variations of micro-channel base heat flux,  $q''_{base}$ , and base temperature,  $T_{base}$ , are obtained by assuming one-dimensional heat conduction along the direction perpendicular to the top surface of the copper block [24]. In the superheated vapor region near the channel inlet, sensible heat loss of FC-72 can be calculated from the following energy balance,

$$q''_{base}(W_{ch} + W_s)\Delta z = \frac{\dot{m}}{N} c_{p,g} \Delta T_f. \quad (1)$$

The onset of two-phase condensation is calculated to occur at the distance from the channel inlet where the fluid temperature reaches the saturation temperature corresponding to the local pressure. The quality in the superheated region can be determined from

$$x = 1 + \frac{c_{p,g}(T_f - T_{sat})}{h_{fg}}, \quad (2)$$

where  $T_f$  and  $T_{sat}$  are the local bulk fluid and saturation temperatures, respectively.

### 3.3. Control volume analysis

To develop a theoretical control-volume-based model, mass and momentum conservation are first applied to control volumes encompassing the liquid film and the vapor core separately. For the two-phase condensing region, mass conservation for the liquid film and the vapor core can be expressed, respectively, as

$$\frac{d\dot{m}_f}{dz} - \Gamma_{fg} = 0 \quad (3)$$

and

$$\frac{d\dot{m}_g}{dz} + \Gamma_{fg} = 0, \quad (4)$$

where the mass flow rates of the liquid film and the vapor core, and the rate of mass transfer due to condensation are defined, respectively, as

$$\dot{m}_f = 2\rho_f \int_0^\delta u_f [(H_{ch} - 2y) + (W_{ch} - 2y)] dy, \quad (5)$$

$$\dot{m}_g = \rho_g \bar{u}_g (W_{ch} - 2\delta)(H_{ch} - 2\delta) \quad (6)$$

and

$$\Gamma_{fg} = \frac{q''_w(2H_{ch} + W_{ch})}{h_{fg}} = \frac{q''_{base}(W_{ch} + W_s)}{h_{fg}}. \quad (7)$$

Applying momentum conservation to the liquid film element illustrated in Fig. 6(a) yields

$$-\Gamma_{fg} u_i \Delta z = PA_{f,*} - \left( P + \frac{dP}{dz} \Delta z \right) A_{f,*} - \tau P_{f,y} \Delta z + \tau_i P_{f,\delta} \Delta z, \quad (8)$$

where the flow area,  $A_{f,*}$ , local perimeter,  $P_{f,y}$ , and interfacial perimeter,  $P_{f,\delta}$ , can be expressed, respectively, as

$$A_{f,*} = (H_{ch} - 2y)(W_{ch} - 2y) - (H_{ch} - 2\delta)(W_{ch} - 2\delta), \quad (9)$$

$$P_{f,y} = 2[(H_{ch} - 2y) + (W_{ch} - 2y)] \quad (10)$$

and

$$P_{f,\delta} = 2[(H_{ch} - 2\delta) + (W_{ch} - 2\delta)]. \quad (11)$$

Rearranging Eq. (8) gives

$$\tau = \left( -\frac{dP}{dz} \right) \frac{A_{f,*}}{P_{f,y}} + \frac{\tau_i P_{f,\delta} + \Gamma_{fg} u_i}{P_{f,y}}. \quad (12)$$

Allowing for turbulence in the condensing film, the local shear stress in the film can be expressed as

$$\tau = \mu_f \left( 1 + \frac{\varepsilon_m}{\nu_f} \right) \frac{du_f}{dy}, \quad (13)$$

where  $\varepsilon_m$  is the eddy momentum diffusivity. Substituting Eq. (13) into Eq. (12) and integrating yield the velocity profile across the liquid film.

$$u_f(y) = \frac{\delta}{\mu_f} \left( -\frac{dP}{dz} \right) \int_0^{y/\delta} \frac{A_{f,*}}{P_{f,y}} \left( 1 + \frac{\varepsilon_m}{\nu_f} \right)^{-1} d\left(\frac{y}{\delta}\right) + \frac{\delta}{\mu_f} (\tau_i P_{f,\delta} + \Gamma_{fg} u_i) \int_0^{y/\delta} \frac{1}{P_{f,y}} \left( 1 + \frac{\varepsilon_m}{\nu_f} \right)^{-1} d\left(\frac{y}{\delta}\right). \quad (14)$$

The interfacial velocity can be determined by setting  $y = \delta$  in Eq. (14).

$$u_i = \frac{\left( -\frac{dP}{dz} \right) \int_0^1 \frac{A_{f,*}}{P_{f,y}} \left( 1 + \frac{\varepsilon_m}{\nu_f} \right)^{-1} d\left(\frac{y}{\delta}\right) + \tau_i P_{f,\delta} \int_0^1 \frac{1}{P_{f,y}} \left( 1 + \frac{\varepsilon_m}{\nu_f} \right)^{-1} d\left(\frac{y}{\delta}\right)}{\frac{\mu_f}{\delta} - \Gamma_{fg} \int_0^1 \frac{1}{P_{f,y}} \left( 1 + \frac{\varepsilon_m}{\nu_f} \right)^{-1} d\left(\frac{y}{\delta}\right)}. \quad (15)$$

Substituting Eq. (14) into Eq. (5) yields the following relation for pressure gradient,

$$-\frac{dP}{dz} = \frac{\frac{\mu_f \dot{m}_f}{\rho_f \delta^2} - (\tau_i P_{f,\delta} + \Gamma_{fg} u_i) \int_0^1 \left[ P_{f,y} \int_0^{y/\delta} \frac{1}{P_{f,y}} \left( 1 + \frac{\varepsilon_m}{\nu_f} \right)^{-1} d\left(\frac{y}{\delta}\right) \right] d\left(\frac{y}{\delta}\right)}{\int_0^1 \left[ P_{f,y} \int_0^{y/\delta} \frac{A_{f,*}}{P_{f,y}} \left( 1 + \frac{\varepsilon_m}{\nu_f} \right)^{-1} d\left(\frac{y}{\delta}\right) \right] d\left(\frac{y}{\delta}\right)}. \quad (16)$$

The double integral terms in the above equation can be expanded as follows,

$$\int_0^1 \left[ P_{f,y} \int_0^{y/\delta} F(y) d\left(\frac{y}{\delta}\right) \right] d\left(\frac{y}{\delta}\right) = 2(H_{ch} + W_{ch}) \int_0^1 \left[ \int_0^{y/\delta} F(y) d\left(\frac{y}{\delta}\right) \right] d\left(\frac{y}{\delta}\right) + 4\delta \int_0^1 \left[ \left(\frac{y}{\delta}\right)^2 - 1 \right] F(y) d\left(\frac{y}{\delta}\right). \quad (17)$$

Applying momentum conservation to a rectangular element of the vapor core illustrated in Fig. 6(b) yields

$$\rho_g \bar{u}_g^2 A_g + \frac{d(\rho_g \bar{u}_g^2 A_g)}{dz} \Delta z - \rho_g \bar{u}_g A_g + \Gamma_{fg} u_i \Delta z = PA_g - \left[ PA_g + \frac{d(PA_g)}{dz} \Delta z \right] - \tau_i P_{f,\delta} \Delta z + \left( P + \frac{1}{2} \frac{dP}{dz} \Delta z \right) \frac{dA_g}{dz} \Delta z. \quad (18)$$

Rearranging Eq. (18) and neglecting the second order term of  $\Delta z$  yield the following relation for interfacial shear stress between the condensing film and vapor core,

$$\tau_i = \frac{1}{P_{f,\delta}} \left[ A_g \left( -\frac{dP}{dz} \right) - \frac{d(\rho_g \bar{u}_g^2 A_g)}{dz} - \Gamma_{fg} u_i \right], \quad (19)$$

where the flow area of the vapor core is  $A_g = (W_{ch} - 2\delta)(H_{ch} - 2\delta)$ .

The interfacial shear stress is the result of velocity differences between the vapor core and interface, modified by the influence of interfacial momentum transfer due to condensation along the vapor–liquid interface due to condensation; the later is obtained using a treatment by Wallis [25],

$$\tau_i = f_i \left[ \frac{1}{2} \rho_g (\bar{u}_g - u_i)^2 \right] + \frac{(\bar{u}_g - u_i) \Gamma_{fg}}{2P_{f,\delta}}. \quad (20)$$

The interfacial friction factor,  $f_i$ , can be determined from relations by Shah and London [26],

$$f_i Re_c = 24 \left( 1 - 1.3553\beta_c + 1.9467\beta_c^2 - 1.7012\beta_c^3 + 0.9564\beta_c^4 - 0.2537\beta_c^5 \right) \quad (21a)$$

$$f_i = 0.079 Re_c^{-0.25} \quad \text{for } 2,000 \leq Re_c < 20,000 \quad (21b)$$

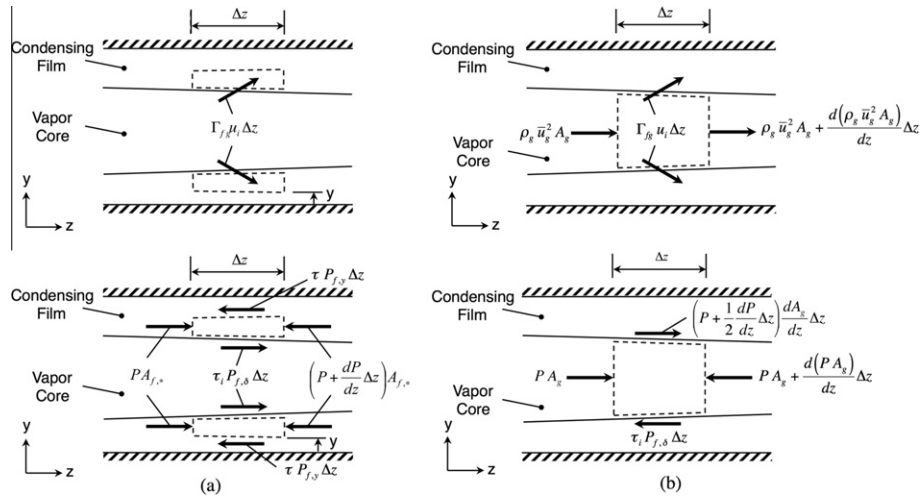


Fig. 6. Momentum and force components for (a) liquid film control volume and (b) vapor core control volume.

and

$$f_i = 0.046 Re_c^{-0.2}, \quad \text{for } Re_c \geq 20,000, \quad (21c)$$

where  $\beta_c$ ,  $Re_c$ , and  $D_{h,c}$  are the aspect ratio, effective Reynolds number, and hydraulic diameter of the vapor core, respectively, which are given by

$$\beta_c = \frac{W_{ch} - 2\delta}{H_{ch} - 2\delta}, \quad (22)$$

$$Re_c = \frac{\rho_g(\bar{u}_g - u_i)D_{h,c}}{\mu_g} \quad (23)$$

and

$$D_{h,c} = \frac{4A_g}{P_{f,\delta}}. \quad (24)$$

### 3.4. Turbulence model

Eq. (13) can be expressed in nondimensional form as

$$\frac{\tau}{\tau_w} = \left(1 + \frac{\varepsilon_m}{\nu_f}\right) \frac{du^+}{dy^+}, \quad (25)$$

where

$$u^+ = \frac{u}{u^*}, \quad (26)$$

$$y^+ = \frac{yu^*}{\nu_f} \quad (27)$$

and

$$u^* = \left(\frac{\tau_w}{\rho_f}\right)^{0.5}. \quad (28)$$

Based on the Prandtl mixing length theory, the eddy diffusivity can be expressed in terms of the turbulent mixing length according to the relation

$$\frac{\varepsilon_m}{\nu_f} = l^{+2} \frac{du^+}{dy^+}. \quad (29)$$

A turbulent mixing length relation originally proposed by Van Driest [27] was modified by Kays [28,29] to the following form,

$$l^+ = Ky^+ \left[1 - \exp\left(-\sqrt{\frac{\tau}{\tau_w A^+}}\right)\right], \quad (30)$$

where the Von-Karman constant of  $K = 0.4$  is used for all subsequent calculations, and the constant  $A^+$  is given by [28,29],

$$A^+ = 26 \left(1 + 30.18 \mu_f \rho_f^{-0.5} \tau_w^{-1.5} \frac{dP}{dz}\right)^{-1}. \quad (31)$$

Substituting Eqs. (25) and (30) into Eq. (29) yields the following eddy diffusivity profile,

$$\frac{\varepsilon_m}{\nu_f} = -\frac{1}{2} + \frac{1}{2} \sqrt{1 + 4K^2 y^{+2} \left[1 - \exp\left(-\sqrt{\frac{\tau}{\tau_w A^+}} y^+\right)\right]^2} \frac{\tau}{\tau_w}. \quad (32)$$

In order to account for interfacial dampening in the condensation film due to surface tension suppression of turbulent eddies, a dampening term,  $(1 - y^+/\delta^+)^n$ , is included in the above eddy diffusivity profile, where the influence of the parameter  $n$  will be discussed later. The complete form of eddy momentum diffusivity distribution in the shear-driven film is expressed as

$$\frac{\varepsilon_m}{\nu_f} = -\frac{1}{2} + \frac{1}{2} \sqrt{1 + 4K^2 y^{+2} \left[1 - \exp\left(-\sqrt{\frac{\tau}{\tau_w A^+}} y^+\right)\right]^2} \frac{\tau}{\tau_w} \left(1 - \frac{y^+}{\delta^+}\right)^n, \quad (33)$$

where, based on Eq. (12),

$$\frac{\tau}{\tau_w} = \frac{2(H_{ch} + W_{ch})}{P_{f,y}} \frac{\left(-\frac{dP}{dz}\right)A_{f,*} + \tau_i P_{f,\delta} + \Gamma_{fg} u_i}{\left(-\frac{dP}{dz}\right)[2\delta(H_{ch} + W_{ch}) - 4\delta^2] + \tau_i P_{f,\delta} + \Gamma_{fg} u_i}. \quad (34)$$

### 3.5. Determination of heat transfer coefficient

Heat flux across the liquid film is related to the liquid temperature gradient by the relation,

$$\frac{q''}{q''_w} = \left(\frac{1}{Pr_T} + \frac{1}{Pr_T} \frac{\varepsilon_m}{\nu_f}\right) \frac{dT^+}{dy^+}, \quad (35)$$

where  $T^+$  is the dimensionless temperature defined as

$$T^+ = \frac{\rho_f C_{p,f} u^* (T - T_w)}{q''_w} \quad (36)$$

and  $Pr_T$  is the turbulent Prandtl number ( $\varepsilon_m/\sum_h$ ), which, as discussed by Mudawar and El-Masri [21], can be evaluated from the experimental data of Ueda et al. [20],

$$Pr_T = 1.4 \exp\left(-15 \frac{y^+}{\delta^+}\right) + 0.66. \quad (37)$$

Integrating Eq. (35), the dimensionless temperature profile across the liquid film can be expressed as

$$T^+ = \int_0^{y^+} \frac{q''}{q''_w} \left( \frac{1}{Pr_f} + \frac{1}{Pr_T} \frac{\varepsilon_m}{\nu_f} \right)^{-1} dy^+ \quad (38)$$

Under three-sided cooling conditions for trapezoidal micro-channels, Quan et al. [30] developed a semi-analytical model for the annular condensation heat transfer coefficient based on the assumption of uniform circumferential heat flux in the vapor-liquid interface. Adopting a heat flux relation similar to that of Quan et al., the present model for condensation in rectangular micro-channels with three-sided cooling walls employs the following energy balance.

$$\frac{q''}{q''_w} = \frac{2H_{ch} + W_{ch}}{2[(H_{ch} - 2y) + (W_{ch} - 2y)]} \quad (39)$$

Therefore, the local condensation heat transfer coefficient can be expressed as

$$h_{tp} = \frac{q''_w}{(T_{sat} - T_w)} = \frac{\rho_f c_{p,f} u^*}{T_{\delta}^+} = \frac{\rho_f c_{p,f} u^*}{\int_0^{\delta^+} \frac{q''}{q''_w} \left( \frac{1}{Pr_f} + \frac{1}{Pr_T} \frac{\varepsilon_m}{\nu_f} \right)^{-1} dy^+} \quad (40)$$

### 3.6. Calculation procedure

The model equations presented in the previous sections are solved numerically using a finite difference technique. The axial distance is divided into small  $\Delta z$  increments and calculations are repeated starting at the upstream location where the film is initiated. The calculation procedure is as follows:

1.  $\varepsilon_m/\nu_f$  and  $\delta$  are both set to zero at the film's upstream location.
2. An initial guess of  $\varepsilon_m/\nu_f$  at the next  $\Delta z$  location is made with the values of the wall shear stress,  $\tau_w$ , interfacial shear,  $\tau_i$ , interfacial velocity,  $u_i$ , and pressure gradient,  $-dP/dz$ , at the node immediately upstream using Eq. (33).
3. An initial value of the film thickness  $\delta$  is assumed.
4. The interfacial velocity,  $u_i$ , interfacial friction factor,  $f_i$ , interfacial shear,  $\tau_i$ , and pressure gradient,  $-dP/dz$ , are calculated using Eq. (15), (21), (20) and (16), respectively.
5. Convergence is checked by comparing the two sides of Eq. (19). If the sides are not equal,  $\varepsilon_m/\nu_f$  is updated with new values of  $\tau_w$ ,  $\tau_i$ ,  $u_i$ , and  $-dP/dz$  at the present node, and steps (3)–(5) are repeated until the correct value for  $\delta$  is found.
6. The values of  $\varepsilon_m/\nu_f$ ,  $u^+$ ,  $T^+$ , and  $h_{tp}$  are calculated using Eqs. (33), (14), (38), and (40), respectively. Steps 2–6 are then repeated for the next downstream node. The procedure is continued until the last node is reached.

### 3.7. Simplified model

Since the thickness of the condensing film is generally small compared to the micro-channel hydraulic diameter, a simplified model can be derived using the following assumption,

$$P_{f,y} = P_{f,\delta} = P_f = 2(H_{ch} + W_{ch}). \quad (41)$$

Then, the flow area and mass flow rate of the liquid film can be expressed, respectively, as

$$A_{f,*} = P_f(\delta - y) \quad (42)$$

and

$$\dot{m}_f = \rho_f P_f \int_0^{\delta} u_f dy. \quad (43)$$

Applying momentum conservation to a rectangular annular element of the liquid film yields the following shear stress relation,

$$\frac{\tau}{\tau_w} = \frac{\left(-\frac{dP}{dz}\right)(\delta - y) + \tau_i \frac{\Gamma_{fg} u_i}{P_f}}{\left(-\frac{dP}{dz}\right)\delta + \tau_i + \frac{\Gamma_{fg} u_i}{P_f}} \quad (44)$$

Similar to the procedure used in previous section, the velocity profile, interfacial velocity, and pressure gradient can be simplified, respectively, as

$$u_f(y) = \frac{\delta^2}{\mu_f} \left(-\frac{dP}{dz}\right) \int_0^{y/\delta} \left(1 - \frac{y}{\delta}\right) \left(1 + \frac{\varepsilon_m}{\nu_f}\right)^{-1} d\left(\frac{y}{\delta}\right) + \frac{\delta}{\mu_f} \left(\tau_i + \frac{\Gamma_{fg} u_i}{P_f}\right) \int_0^{y/\delta} \left(1 + \frac{\varepsilon_m}{\nu_f}\right)^{-1} d\left(\frac{y}{\delta}\right), \quad (45)$$

$$u_i = \frac{\delta \left(-\frac{dP}{dz}\right) \int_0^1 \left(1 - \frac{y}{\delta}\right) \left(1 + \frac{\varepsilon}{\nu_f}\right)^{-1} d\left(\frac{y}{\delta}\right) + \tau_i \int_0^1 \left(1 + \frac{\varepsilon_m}{\nu_f}\right)^{-1} d\left(\frac{y}{\delta}\right)}{\frac{\mu_f}{\delta} - \frac{\Gamma_{fg}}{P_f} \int_0^1 \left(1 + \frac{\varepsilon_m}{\nu_f}\right)^{-1} d\left(\frac{y}{\delta}\right)}, \quad (46)$$

and

$$-\frac{dP}{dz} = \frac{\frac{\mu_f \dot{m}_f}{\rho_f P_f \delta^2} - \left(\tau_i + \frac{\Gamma_{fg} u_i}{P_f}\right) \int_0^1 \left[\int_0^{y/\delta} \left(1 + \frac{\varepsilon_m}{\nu_f}\right)^{-1} d\left(\frac{y}{\delta}\right)\right] d\left(\frac{y}{\delta}\right)}{\delta \int_0^1 \left[\int_0^{y/\delta} \left(1 - \frac{y}{\delta}\right) \left(1 + \frac{\varepsilon_m}{\nu_f}\right)^{-1} d\left(\frac{y}{\delta}\right)\right] d\left(\frac{y}{\delta}\right)}. \quad (47)$$

As discussed later, the predictive differences of pressure drop average only 1.8%, with a maximum difference of 3.8%; corresponding differences for the average heat transfer coefficient are 0.5% and 1.0%, respectively. Although both models yield very close results, all of the subsequent calculations are based on the complete model unless indicated otherwise.

## 4. Model results

### 4.1. Effect of turbulent dampening term

Mudawar and El-Masri [21] examined the interfacial dampening effects on the turbulence mixing length for free-falling liquid films. They derived the following turbulence mixing length profile based on an eddy-diffusivity profile measured experimentally by Ueda et al. [20] for open-channel flows,

$$l^+ = Ky^+ \left[ 1 - \exp\left(-\sqrt{1 - \frac{y^+ y^+}{\delta^+ A^+}}\right) \right] \sqrt{1 - \frac{y^+}{\delta^+}} \quad (48)$$

Substituting Eqs. (25) and (48) into Eq. (29) gives the following eddy diffusivity profile,

$$\frac{\varepsilon_m}{\nu_f} = -\frac{1}{2} + \frac{1}{2} \sqrt{1 + 4K^2 y^{+2} \left[ 1 - \exp\left(-\sqrt{1 - \frac{y^+ y^+}{\delta^+ A^+}}\right) \right]^2 \left(1 - \frac{y^+}{\delta^+}\right) \frac{\tau}{\tau_w}} \quad (49)$$

It should be noted that, since the mixing length profile of Mudawar and El-Masri is valid only for  $\varepsilon_m/\nu_f > 1$  and negligible interfacial shear stress, their eddy diffusivity profile cannot be used for micro-channel condensation, where turbulence effects are relatively weak and interfacial shear is the primary driving force for film motion.

The present eddy diffusivity profile given by Eq. (33) yielded values for dimensionless film thickness,  $y^+ = \delta^+$ , up to about 16 at the micro-channel exit, which is close to the outer edge of the viscous sublayer for typical turbulent flows. The present diffusivity profile is justified by the fact that Van-Driest models are applicable near the solid wall region where  $y^+ \leq 30$ . The dampening coefficient,  $(1 - y^+/\delta^+)^n$ , in Eq. (33) accounts for the vanishing turbulence effects, if any, at the film interface. Without this term, the conventional Van-Driest profile cannot account for the interfacial dampening.

Using Eq. (33), four different powers of the dampening term,  $(1 - y^+/\delta^+)^n$ ,  $n = 0$  (corresponding to zero dampening as expressed by Eq. (32)), 0.1, 0.5, and 1.0, are examined. Fig. 7(a), (b) and (c) show the impact of the dampening term on the distributions of eddy diffusivity, velocity, and temperature, respectively, across the FC-72 film for  $G = 367 \text{ kg/m}^2 \text{ s}$  and  $\dot{m}_w = 6 \text{ g/s}$ . Fig. 7(a) shows that, without the dampening term, the eddy diffusivity increases monotonically with increasing  $y^+$ , while with the dampening term,

the eddy diffusivity is reduced to zero at the film interface. Increasing the magnitude of the exponent  $n$  causes the effect of interfacial dampening to penetrate deeper towards the wall. Fig. 7(b) shows that increasing  $n$  increases the liquid velocity near the interface. Fig. 7(c) shows a similar trend of increasing liquid temperature near the interface with increasing  $n$ . An interesting aspect of the temperature profile is the unusual temperature rise in the immediate vicinity of the film interface caused by the eddy diffusivity term in Eq. (35) approaching zero.

Although Fig. 8(a) shows that different  $n$  values yield fairly similar film thickness results, Fig. 8(b) shows that increasing the power increases the temperature gradient near the interface, which can produce a measurable decrease in the heat transfer coefficient. An optimum value of  $n = 0.1$  was ascertained by comparing predictions of the local as well as average heat transfer coefficients with the experimental data of Kim and Mudawar [23]. This value is therefore used for all of subsequent calculations.

#### 4.2. Effects of mass velocity

Fig. 9 shows predicted variations of several film parameters with quality for different FC-72 mass velocities at a constant water flow rate of 6 g/s. Liquid film and vapor core Reynolds numbers are defined, respectively, as

$$Re_f = \frac{4\rho_f \bar{u}_f \delta}{\mu_f} \tag{50}$$

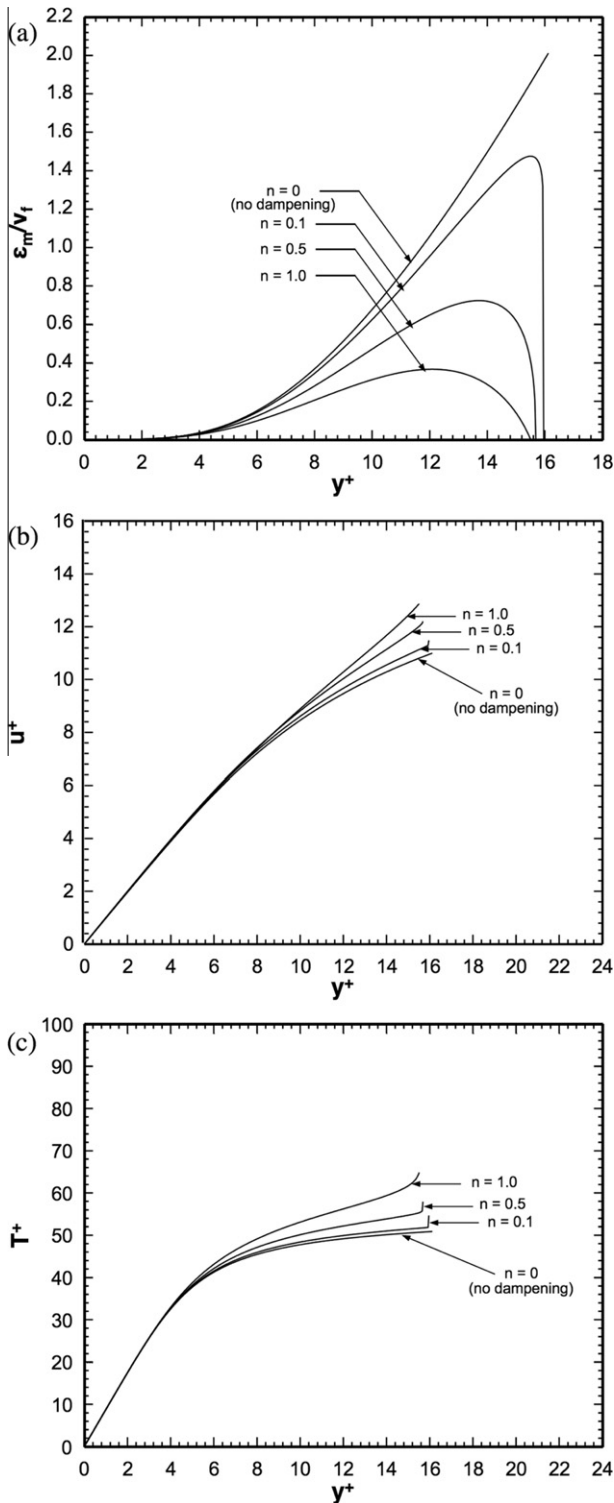


Fig. 7. Effects of interfacial dampening term on (a) eddy momentum diffusivity, (b) velocity, and (c) temperature distributions across condensing FC-72 film for  $G = 367 \text{ kg/m}^2 \text{ s}$ , and  $\dot{m}_w = 6 \text{ g/s}$ .

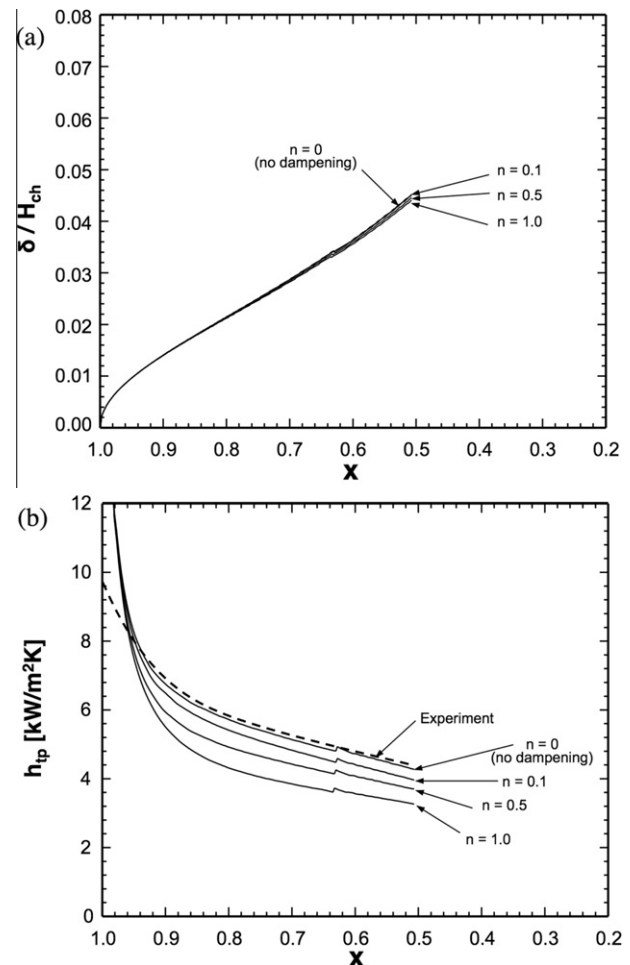


Fig. 8. Effects of interfacial dampening term on variations of (a) liquid film thickness, and (b) local heat transfer coefficient with quality for  $G = 367 \text{ kg/m}^2 \text{ s}$  and  $\dot{m}_w = 6 \text{ g/s}$ .

and

$$Re_g = \frac{\rho_g \bar{u}_g D_{h,c}}{\mu_g}, \tag{51}$$

where the mean liquid film velocity,  $\bar{u}_f$ , is expressed as

$$\bar{u}_f = \frac{\dot{m}_f}{\rho_f [W_{ch} H_{ch} - (W_{ch} - 2\delta)(H_{ch} - 2\delta)]}. \tag{52}$$

Peterson et al. [31] proposed the following correlation for transition from laminar to turbulent film flow for downward flowing films,

$$Re_{f,tr} = 4080 \left[ (1 + 0.31 \tau_i^{*1.07}) (1.18 Pr_f^{0.87} - 0.23) \right]^{-1}, \tag{53}$$

where the nondimensional interfacial shear stress is defined as

$$\tau_i^* = \frac{\tau_i}{\rho_f g (v_f^2/g)^{1/3}}. \tag{54}$$

Based on this correlation, transition to turbulent film flow is estimated to occur at very low film Reynolds numbers when the values of interfacial shear and liquid Prandtl number are high. Using values relevant to the present study, with  $\tau_i = 15$  Pa ( $\tau_i^* = 50$ ) and  $T_{sat} = 60$  °C ( $Pr_f = 8.66$ ), Eq. (54) yields a transitional Reynolds number of  $Re_{f,tr} = 25$ . Therefore, although  $Re_f$  values for the present study are relatively small (less than 400), strong interfacial shear promotes turbulence film flow for most operating conditions. This fact supports assumption (11) used in the development of the present model.

Fig. 9(a), (b) and (c) show that increasing the mass velocity of FC-72 increases the film Reynolds number, vapor core Reynolds number and interfacial shear stress, respectively. The slight discontinuities in the shear stress plots are caused by the different ranges of the effective Reynolds number of the vapor core,  $Re_c$ , as indicated by (21)(a)–(c). Fig. 9(d) shows the film thickness decreasing with increasing mass velocity because of the increased interfacial shear. Fig. 9(e) shows how the decreasing film thickness with

increased mass velocity increases the heat transfer coefficient. For each mass velocity, Fig. 9(e) shows that the heat transfer coefficient is greatest where the film is first initiated and decreases monotonically downstream as the film thickens due to gradual condensation along the channel.

### 4.3. Validation of model predictions

Fig. 10(a) compares pressure drop predictions with pressure drop data measured by Kim et al. [22] for different water mass flow rates and FC-72 mass velocities of  $G = 248, 306, \text{ and } 367$  kg/m<sup>2</sup> s. Details of the data reduction used to evaluate total pressure drop between the inlet and outlet plenums are provided in [22]. Fig. 10(a) proves that the model accurately captures the measured pressure drop in both magnitude and trend.

Fig. 10(b) compares predictions of the present model and nine prior separated flow correlations against the present pressure drop FC-72 data. The correlations include six specifically developed for mini/micro-channels; the other three are intended for macro-channels. All three macro-channel correlations significantly over predict the FC-72 micro-channel data. Among the mini/micro-channel correlations, those by Mishima and Hibiki [32] and Nino et al. [37], which are both based on air–water adiabatic flow, show fair predictions. Interestingly, these predictions are superior to those of the correlation by Tran et al. [33], which was developed specifically for flow boiling in small channels. This supports the fact that, in the absence of droplet entrainment and deposition effects, micro-channel condensing flows are closer in flow structure (on a local basis) to adiabatic than boiling micro-channel flows as depicted in Fig. 4(a). Overall, Fig. 10(b) shows the excellent predictive capability of the present theoretical model, evidenced by a MAE of 3.6%.

Fig. 11(a) compares predictions of the present model and average FC-72 heat transfer coefficient data for different FC-72 mass velocities and water flow rates. The model does capture the experimental trends relative to FC-72 mass velocity and water mass flow rate. Deviations between predicted and measure values may be

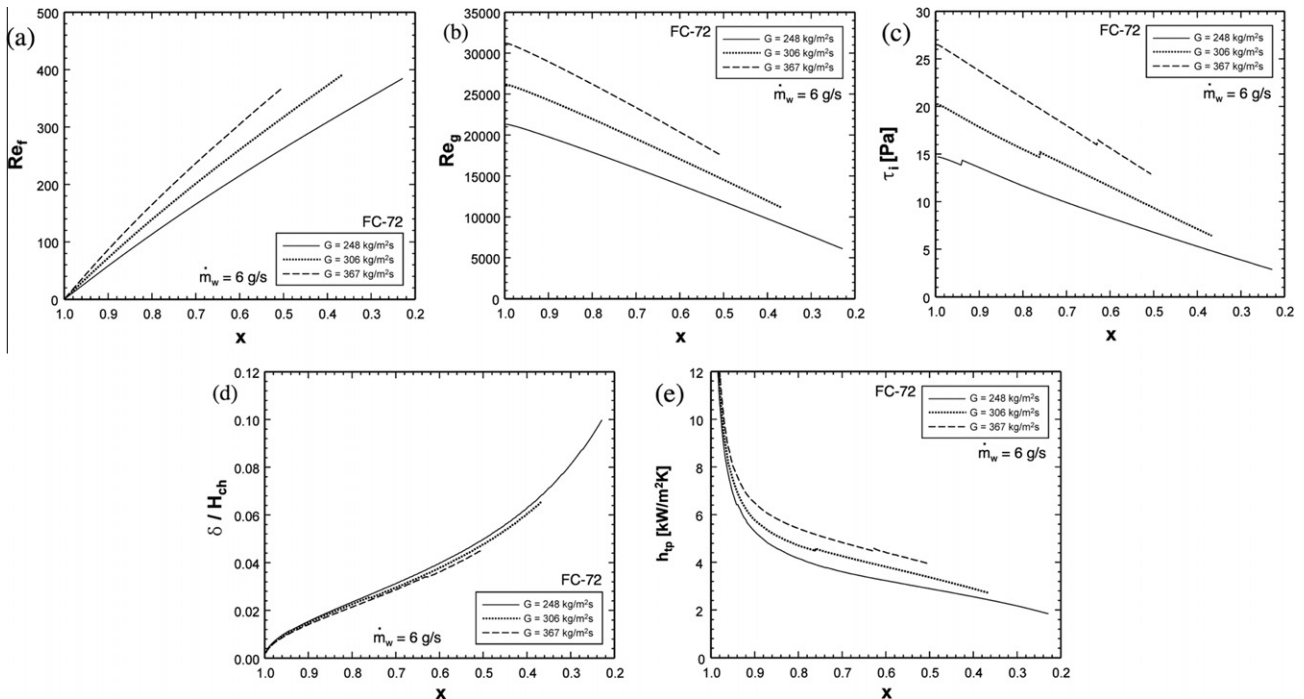


Fig. 9. Variations of (a) liquid film Reynolds number, (b) vapor core Reynolds number, (c) interfacial shear stress, (d) liquid film thickness, and (e) local heat transfer coefficient with quality for different FC-72 mass velocities and  $\dot{m}_w = 6$  g/s.

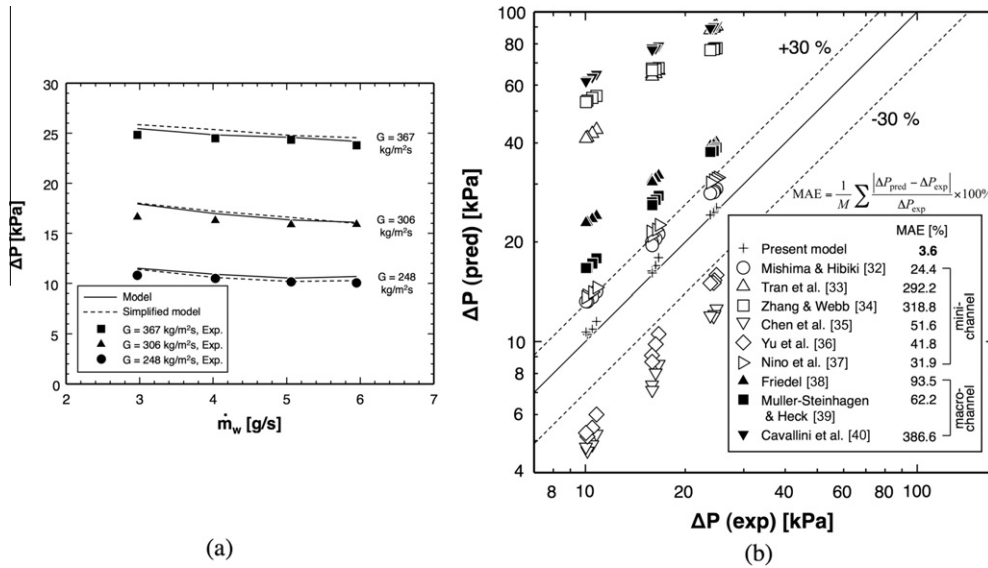


Fig. 10. (a) Variations of predicted and measured total pressure drops with water mass flow rate for different FC-72 mass velocities. (b) Comparison of measured FC-72 total pressure drop data with predictions of present model and previous correlations. (See above mentioned references for further information.)

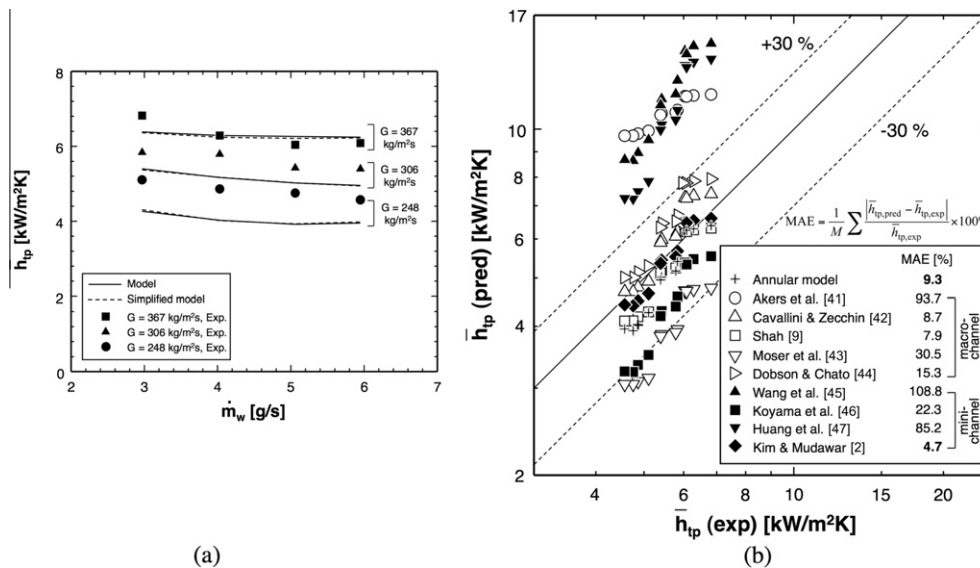


Fig. 11. (a) Variations of predicted and measured average heat transfer coefficients with water mass flow rate for different FC-72 mass velocities. (b) Comparison of measured FC-72 average condensation heat transfer coefficient data with predictions of present annular model and previous annular condensation heat transfer correlations. (See above mentioned references for further information.)

related to film waviness, which is more prevalent for the lower mass velocity [22]. Waviness can increase the heat transfer coefficient in two ways, by increasing liquid–vapor interfacial area and by decreasing mean film thickness due to the interfacial waves propagating slightly faster than the rest of the liquid. Another reason for the deviations between predicted and measured values is the circumferential non-uniformity of the liquid film, with more liquid driven towards the corners, thinning the film along the flat walls of the micro-channel. Despite the low surface tension of FC-72, corner effects can slightly influence the mean film thickness. Another source of predictive error may be minor stratification in the horizontal channels, especially at low mass velocities.

Fig. 11(b) compares predictions of the present model and nine prior separated flow correlations against the present average heat transfer coefficient FC-72 data. The correlations include four specifically developed for mini/micro-channels; the other five are

intended for macro-channels. Interestingly, excepting the correlation by Akers et al. [41], most macro-channel correlations provide good predictions of the present data. With a MAE of 4.7%, the recent correlation by Kim and Mudawar [23] shows the best predictive capability. Nearly as accurate, the present theoretical model predicts the data with a MAE of 9.3%.

Fig. 12 compares predictions of the present model and prior correlations with the present local heat transfer coefficient data for three FC-72 mass velocities. Notice that, despite their low MAE in predicting the average heat transfer coefficient data, the correlations of Shah [9], Cavallini and Zecchin [42], and Dobson and Chato [44], do not accurately capture the variation of local heat transfer coefficient with quality. Overall, both the present theoretical model and the recent correlation by Kim and Mudawar [23] show good accuracy in predicting the measured trend of local heat transfer coefficient with quality.

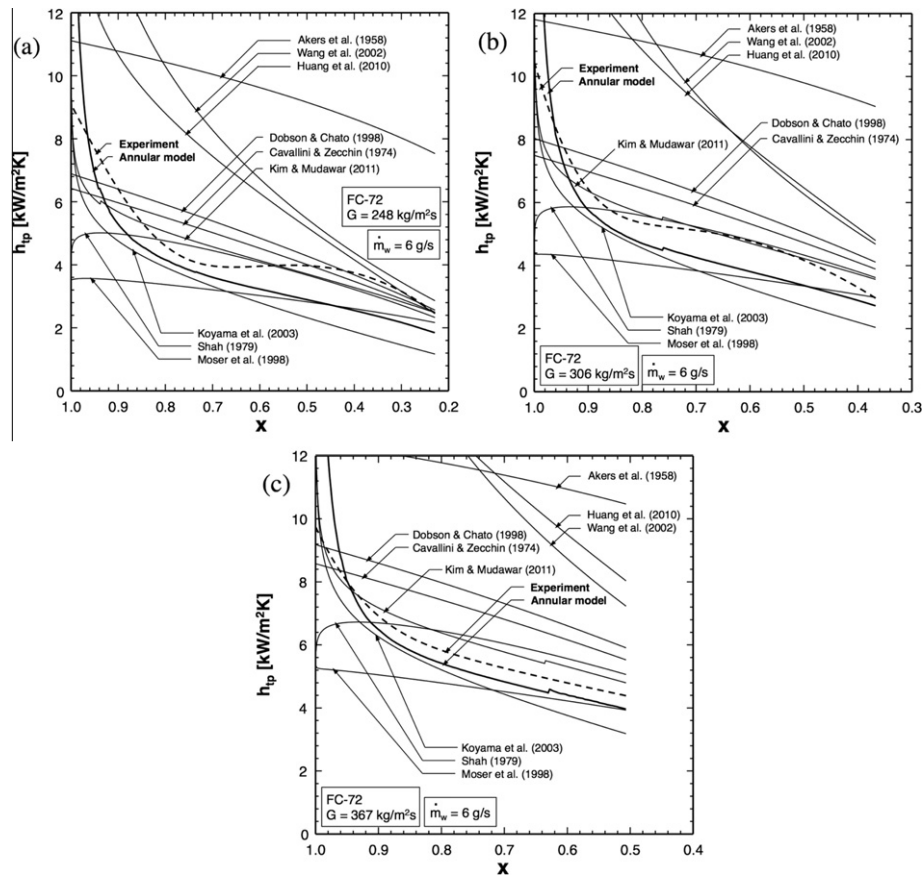


**Fig. 12.** Comparison of measured FC-72 local heat transfer coefficient data with predictions of present model and previous annular condensation heat transfer correlations for  $\dot{m}_w = 6$  g/s with (a)  $G = 248$  kg/m<sup>2</sup> s, (b)  $G = 306$  kg/m<sup>2</sup> s, and (c)  $G = 367$  kg/m<sup>2</sup> s.

## 5. Conclusions

This study examined the pressure drop and heat transfer characteristics of annular condensation in rectangular micro-channels with three-sided cooling walls. Central to the study is the development of a theoretical control-volume-based model, which is based on the assumptions of smooth interface between the annular liquid film and vapor core, and uniform film thickness around the channel's circumference. The model predictions are compared with experimental micro-channel pressure drop and condensation heat transfer data for FC-72. This study also explored the accuracy of prior separated flow correlations in predicting the same data. Key conclusions from the study are as follows.

- (1) Unlike flow boiling, droplet entrainment and deposition effects are nonexistent in micro-channel annular condensing flows.
- (2) Annular condensation can be divided into two separate regions, an upstream smooth-annular region and a downstream wavy-annular region. While the annular film in the wavy-annular regime is marred by interfacial waves, these waves are fairly small in profile and do not evolve into large waves, nor do they appear to have an appreciable influence on the film's transport behavior.
- (3) For shear-driven films, transition from laminar to turbulent film flow may occur at unusually small film Reynolds numbers. Turbulent effects must therefore be incorporated when modeling the transport behavior of annular condensing films.
- (4) Interfacial dampening of turbulent eddies is accurately accounted for in the new model with the aid of a new eddy diffusivity model specifically tailored to turbulent shear-drive films.

- (5) While some of the previous separated flow correlations do provide accurate predictions of the average heat transfer coefficient, they fail to predict axial variations of the local condensation heat transfer coefficient.
- (6) The present model accurately predicts the pressure drop and heat transfer coefficient data in both magnitude and trend, evidenced by mean absolute error values of 3.6% and 9.3%, respectively.

## Acknowledgement

The authors are grateful for the support of the Office of Naval Research (ONR) for this study.

## References

- [1] I. Mudawar, D.C. Wadsworth, Critical heat flux from a simulated electronic chip to a confined rectangular impinging jet of dielectric liquid, *Int. J. Heat Mass Transfer* 34 (1991) 1465–1480.
- [2] L. Jiang, M. Wong, Y. Zohar, Forced convection boiling in a microchannel heat sink, *J. Microelectromech. Syst.* 10 (2001) 80–87.
- [3] A. Kawahara, P.M.-Y. Chung, M. Kawaji, Investigation of two-phase flow pattern, void fraction and pressure drop in a microchannel, *Int. J. Multiphase Flow* 28 (2002) 1411–1435.
- [4] L. Lin, R. Ponnappan, Heat transfer characteristics of spray cooling in a closed loop, *Int. J. Heat Mass Transfer* 46 (2003) 3737–3746.
- [5] J. Lee, I. Mudawar, Two-phase flow in high-heat-flux micro-channel heat sink for refrigeration cooling applications: Part II – heat transfer characteristics, *Int. J. Heat Mass Transfer* 48 (2005) 941–955.
- [6] J. Lee, I. Mudawar, Fluid flow and heat transfer characteristics of low temperature two-phase micro-channel heat sinks – Part 1: experimental methods and flow visualization results, *Int. J. Heat Mass Transfer* 51 (2008) 4315–4326.

- [7] J. Lee, I. Mudawar, Fluid flow and heat transfer characteristics of low temperature two-phase micro-channel heat sinks – Part 2: subcooled boiling pressure drop and heat transfer, *Int. J. Heat Mass Transfer* 51 (2008) 4327–4341.
- [8] R.W. Lockhart, R.C. Martinelli, Proposed correlation of data for isothermal two-phase, two-component flow in pipes, *Chem. Eng. Prog.* 45 (1949) 39–48.
- [9] M.M. Shah, A general correlation for heat transfer during film condensation inside pipes, *Int. J. Heat Mass Transfer* 22 (1979) 547–556.
- [10] W. Qu, I. Mudawar, Measurement and prediction of pressure drop in two-phase micro-channel heat sinks, *Int. J. Heat Mass Transfer* 46 (2003) 2737–2753.
- [11] W. Qu, I. Mudawar, Flow boiling heat transfer in two-phase micro-channel heat sinks-II. Annular two-phase flow model, *Int. J. Heat Mass Transfer* 46 (2003) 2773–2784.
- [12] J. Lee, I. Mudawar, Experimental investigation and theoretical model for subcooled flow boiling pressure drop in microchannel heat sinks, *ASME J. Electron. Pack.* 131 (2009) 031008.
- [13] J.C. Sturgis, I. Mudawar, Critical heat flux in a long, rectangular channel subjected to one-sided heating-II. Analysis of critical heat flux data, *Int. J. Heat Mass Transfer* 42 (1999) 1849–1862.
- [14] J.A. Shmerler, I. Mudawar, Local heat transfer coefficient in wavy free-falling turbulent liquid films undergoing uniform sensible heating, *Int. J. Heat Mass Transfer* 31 (1988) 67–77.
- [15] J.A. Shmerler, I. Mudawar, Local evaporative heat transfer coefficient in turbulent free-falling liquid films, *Int. J. Heat Mass Transfer* 31 (1988) 731–742.
- [16] J.E. Koskie, I. Mudawar, W.G. Tiederman, Parallel-wire probes for measurement of thick liquid films, *Int. J. Multiphase Flow* 15 (1989) 521–530.
- [17] T.H. Lyu, I. Mudawar, Statistical investigation of the relationship between interfacial waviness and sensible heat transfer to a falling liquid film, *Int. J. Heat Mass Transfer* 34 (1991) 1451–1464.
- [18] I. Mudawar, R.A. Houpt, Measurement of mass and momentum transport in wavy-laminar falling liquid films, *Int. J. Heat Mass Transfer* 36 (1993) 4151–4162.
- [19] G.L. Hubbard, A.F. Mills, D.K. Chung, Heat transfer across a turbulent falling film with cocurrent vapor flow, *ASME J. Heat Transfer* 98 (1976) 319–320.
- [20] H. Ueda, R. Moller, S. Komori, T. Mizushima, Eddy diffusivity near the free surface of open channel flow, *Int. J. Heat Mass Transfer* 20 (1977) 1127–1136.
- [21] I. Mudawar, M.A. El-Masri, Momentum and heat transfer across freely-falling turbulent liquid films, *Int. J. Multiphase Flow* 12 (1986) 771–790.
- [22] S.M. Kim, J. Kim, I. Mudawar, Flow condensation in parallel rectangular micro-channels – Part 1: Experimental results and assessment of pressure drop correlations, *Int. J. Heat Mass Transfer* 55 (2012) 971–983.
- [23] S.M. Kim, I. Mudawar, Flow condensation in parallel rectangular micro-channels – Part 2: Heat transfer results and correlation technique, *Int. J. Heat Mass Transfer* 55 (2012) 984–994.
- [24] S.M. Kim, I. Mudawar, Analytical heat diffusion models for different micro-channel heat sink cross-sectional geometries, *Int. J. Heat Mass Transfer* 53 (2010) 4002–4016.
- [25] G.B. Wallis, *One Dimensional Two-Phase Flow*, McGraw-Hill, New York, 1969.
- [26] R.K. Shah, A.L. London, *Laminar Flow Forced Convection in Ducts: a Source Book for Compact Heat Exchanger Analytical Data*, vol. 1, Academic press, New York, 1978.
- [27] E.R. Van Driest, On turbulent flow near a wall, *J. Aeronaut. Sci.* 23 (1956) 1007–1011.
- [28] W.M. Kays, Heat transfer to the transpired turbulent boundary layer, *Int. J. Heat Mass Transfer* 15 (1972) 1023–1044.
- [29] W.M. Kays, M.E. Crawford, *Convective Heat and Mass Transfer*, second ed., McGraw-Hill, New York, 1980.
- [30] X. Quan, L. Dong, P. Cheng, Determination of annular condensation heat transfer coefficient of steam in microchannels with trapezoidal cross sections, *Int. J. Heat Mass Transfer* 53 (2010) 3670–3676.
- [31] P.F. Peterson, V.E. Schrock, S.Z. Kuhn, Recent experiments for laminar and turbulent film heat transfer in vertical tubes, *Nucl. Eng. Des.* 175 (1997) 157–166.
- [32] K. Mishima, T. Hibiki, Some characteristics of air–water two-phase flow in small diameter vertical tubes, *Int. J. Multiphase Flow* 22 (1996) 703–712.
- [33] T.N. Tran, M.-C. Chyu, M.W. Wambsganss, D.M. France, Two-phase pressure drop of refrigerants during flow boiling in small channels: an experimental investigation and correlation development, *Int. J. Multiphase Flow* 26 (2000) 1739–1754.
- [34] M. Zhang, R.L. Webb, Correlation of two-phase friction for refrigerants in small-diameter tubes, *Expt. Thermal Fluid Sci.* 25 (2001) 131–139.
- [35] I.Y. Chen, K.-S. Yang, Y.-J. Chang, C.-C. Wang, Two-phase pressure drop of air-water and R-410A in small horizontal tubes, *Int. J. Multiphase Flow* 27 (2001) 1293–1299.
- [36] W. Yu, D.M. France, M.W. Wambsganss, J.R. Hull, Two-phase pressure drop, boiling heat transfer, and critical heat flux to water in a small-diameter horizontal tube, *Int. J. Multiphase Flow* 28 (2002) 927–941.
- [37] V.G. Nino, E.W. Jassim, P.S. Hrnjak, T.A. Newell, Flow regime based model for pressure drop predictions in microchannels, University of Illinois at Urbana-Champaign (2005) ACRC TR-242.
- [38] L. Friedel, Improved friction pressure drop correlations for horizontal and vertical two-phase pipe flow, European Two-phase Group Meeting, Ispra, Italy, 1979, Paper E2.
- [39] H. Muller-Steinhagen, K. Heck, A simple friction pressure drop correlation for two-phase flow in pipes, *Chem. Eng. Process.* 20 (1986) 297–308.
- [40] A. Cavallini, G. Censi, D.D. Col, L. Doretti, G.A. Longo, L. Rossetto, Condensation of halogenated refrigerants inside smooth tubes, *HVAC&R Research* 8 (2002) 429–451.
- [41] W.W. Akers, H.A. Deans, O.K. Crosser, Condensing heat transfer within horizontal tubes, *Chem. Engr. Prog.* 54 (1958) 89–90.
- [42] A. Cavallini, R. Zecchin, A dimensionless correlation for heat transfer in forced convection condensation, in: *Proceedings of the 5th International Heat Transfer Conference*, vol. 3, 1974, pp. 309–313.
- [43] K.W. Moser, R.L. Webb, B. Na, A new equivalent Reynolds number model for condensation in smooth tubes, *ASME J. Heat Transfer* 120 (1998) 410–417.
- [44] M.K. Dobson, J.C. Chato, Condensation in smooth horizontal tubes, *ASME J. Heat Transfer* 120 (1998) 193–213.
- [45] W.-W.W. Wang, T.D. Radcliff, R.N. Christensen, A condensation heat transfer correlation for millimeter-scale tubing with flow regime transition, *Exp. Thermal Fluid Sci.* 26 (2002) 473–485.
- [46] S. Koyama, K. Kuwahara, K. Nakashita, K. Yamamoto, An experimental study on condensation of refrigerant R134a in a multi-port extruded tube, *Int. J. Refrigerat.* 24 (2003) 425–432.
- [47] X. Huang, G. Ding, H. Hu, Y. Zhu, H. Peng, Y. Gao, B. Deng, Influence of oil on flow condensation heat transfer of R410A inside 4.18mm and 1.6mm inner diameter horizontal smooth tubes, *Int. J. Refrigerat.* 33 (2010) 158–169.